



Calix[4]arene based dye-sensitized Pt@UiO-66-NH₂ metal-organic framework for efficient visible-light photocatalytic hydrogen production



Yi-Fan Chen^a, Li-Lin Tan^a, Jun-Min Liu^{a,*}, Su Qin^a, Zhi-Qiang Xie^a, Jian-Feng Huang^a, Yao-Wei Xu^a, Li-Min Xiao^b, Cheng-Yong Su^{a,*}

^a MOE Laboratory of Bioinorganic and Synthetic Chemistry, Lehn Institute of Functional Materials, School of Chemistry, and School of Materials Science and Engineering, Sun Yat-sen University, Guangzhou, 510275, China

^b School of Computer Science and Engineering, Beihang University, Beijing, 100191, China

ARTICLE INFO

Article history:

Received 9 November 2016

Received in revised form 10 January 2017

Accepted 15 January 2017

Available online 20 January 2017

Keywords:

Water splitting

Photocatalytic hydrogen production

Calix[4]arene

Dye sensitization

Metal-organic framework

ABSTRACT

A cone-calix[4]arene dye **Calix-3** with four D- π -A units has been utilized to sensitize Zr-containing metal-organic framework (MOF) embedded with Pt particles, denoted as Pt@UiO-66-NH₂, for photocatalytic H₂ production under visible light irradiation. The structures of UiO-66-NH₂, Pt-loadings, and dye-adsorbed amounts of these photocatalysts are optimized. Comparatively, **Calix-3**-sensitized Pt@UiO-66-NH₂ catalysts with 0.65 wt% of Pt loading and 15.7 μ mol/g of **Calix-3** dye amount exhibit much higher hydrogen production activity (1528 μ mol g⁻¹ h⁻¹ based on the mass of MOF or 236 mmol g⁻¹[Pt] h⁻¹ based on Pt mass) than that sensitized by single D- π -A **M-3** dyes (516 μ mol g⁻¹ h⁻¹ or 24 mmol g⁻¹[Pt] h⁻¹) under the similar photocatalytic conditions, and perform excellent stability during the long-term tests simultaneously. In view of the extremely low Pt loading, the activity based on Pt mass is one of the highest among all the reported MOF-based photocatalytic hydrogen production systems. The enhancement in hydrogen evolution efficiency and stability could be ascribed to lower tendency for aggregation, higher molar absorption coefficients, more efficient electron transfer, and better intrinsic and adsorbed stability of **Calix-3** dyes. This work provides useful insights for future design and synthesis of new functional dye sensitization MOF system for photocatalytic hydrogen production.

© 2017 Elsevier B.V. All rights reserved.

1. Introduction

Hydrogen production from water splitting via photocatalysis, especially in the visible-light spectral region, attracts extensive attention owing to its clean and environmentally friendly use of solar energy. To date, various kinds of photocatalysts, including inorganic semiconducting materials, metal-incorporated zeolite, metal complexes, and other composite photocatalysts, have been discovered for hydrogen evolution reaction (HER) [1–5]. Among them, porous materials permit exposing active sites as much as possible to facilitate the accessibility of photogenerated electrons to substrates and suppress the undesired volume recombination between electrons and holes, making it promising for use as photocatalysts [6–8].

As a class of crystalline porous materials, metal-organic frameworks (MOFs) are assembled by metal clusters interconnected by multidentate organic linkers, which have shown semiconductor-like characters in photocatalysis [9–11]. The metal centers in MOFs can serve as “quantum dots” and the organic linkers as antenna to activate these metal clusters upon photoexcitation [12–14], therefore the short transport length of charge carriers can be achieved in MOFs. Moreover, water molecules can easily diffuse into the pores in MOFs, thus making MOFs as potential active photocatalysts in water reduction for hydrogen production [15]. In 2010, Garcia and co-workers used a highly stable Zr-containing MOFs of UiO-66 and UiO-66-NH₂ for water splitting under UV light irradiation, which opened the door for MOFs to photocatalytic water splitting [16]. Due to the versatile and tailorabile structures, the utilization of solar energy by MOFs, especially in the visible region, could be desirable by selecting ligands or metal centers with visible-light response or post-modifying on the metal ions or the organic ligands [17–21]. For example, porphyrins are versatile functional molecules useful for light harvesting, so a mesoporous zirconium-porphyrin MOF based

* Corresponding authors.

E-mail addresses: liujunm@mail.sysu.edu.cn (J.-M. Liu), cessy@mail.sysu.edu.cn (C.-Y. Su).

on tetrakis(4-carboxyphenyl)- porphyrin (H_2TCPP), was used for visible-light photocatalysis in the presence of triethanolamine as a sacrificial agent [22].

Given the merits of semiconductor-like MOFs further, another alternative promising strategy of integrating the two key components of the photosensitizer and the HER catalyst into MOFs has been adopted to enable light-driven proton reduction [23–25]. Notably, there have been several reports on photocatalysis by loading metal nanoparticles (NPs) into the cavities of a photosensitizing MOF, in which metal NPs act as effective electron acceptors to enable photocatalytic proton reduction with a high efficiency [8,26–28]. In addition, dye-sensitization has become a relatively mature technology for visible-light harvesting when it comes to semiconductor photocatalysts [29,30]. One of the great advantages of the dye sensitization system is ultrafast charge separation producing an electron and a hole at the dye-semiconductor interface, where the spatial charge separation achieved by the electron injection from dye-sensitizers into semiconductors dramatically suppresses the charge recombination of electrons and holes. The charge separation process is thus efficient enough to reach 100% quantum yield in the dye-sensitization system [15]. Nevertheless, the dye-sensitization system for photocatalytic water splitting still remains relatively less efficiency than other systems [31–33]. One of general concerns of dye-sensitization system is the lack of intrinsic stability of dye-sensitizers under photocatalytic reaction in water. Recently, a Rhodamine B sensitized MOF using Pt as a co-catalyst was used for water splitting under visible-light illumination [34], but the poor photostability of Rhodamine B dye makes it not suitable as an efficient photosensitizer [35]. The other factors affecting on the photoelectric conversion efficiency are aggregation of dye molecules on the surface, the co-existing species, and adsorbed stability which depends on the interactions between MOFs and dyes.

Herein, we used low-cost cone-calixarene-based dye (denoted as **Calix-3**, Scheme 1), which has been successfully synthesized and applied in dye-sensitized solar cells [36], as light absorbing antenna and demonstrate an active hydrogen production system over **Calix-3**-sensitized Zr-containing MOF UiO-66-NH_2 (denoted as $\text{Calix-3/Pt@UiO-66-NH}_2$). **Calix-3** was selected for durable photocatalytic H_2 production for the following reasons: (1) **Calix-3** has a cone conformation, which is beneficial to impede dye aggregation; (2) it has four light-harvesting units per molecule, which is not only favorable to achieve high molar extinction coefficients but also ensures more effective electron transfer between the dye and surrounding MOF; (3) it has four $-\text{COOH}$ groups in one molecule

and thus it is expected that a strong hydrogen bonding, besides aromatic stacking and Van Der Waals interaction, exists between UiO-66-NH_2 and dyes, which would increase the stability of the dyes adsorbed on the MOF surface; and (4) it has high photostability and thermostability, which are vital for the photocatalytic water splitting. Furthermore, UiO-66-NH_2 as a stable MOF has been reported for photocatalytic hydrogen production and organic conversion [16,34]. The influences of structure of UiO-66-NH_2 , Pt-loading, dye-adsorbed amount, and the comparison dye **M-3** on the photocatalytic hydrogen production were also investigated. The optimized photocatalytic hydrogen production rate of $\text{Calix-3/Pt@UiO-66-NH}_2$ with 0.65 wt% of Pt loading and $15.7 \mu\text{mol/g}$ of **Calix-3** dye amount was $1528 \mu\text{mol g}^{-1} \text{h}^{-1}$ based on the mass of MOF and $236 \text{ mmol g}^{-1} [\text{Pt}] \text{h}^{-1}$ based on Pt mass, respectively, and the catalysts could be repeatedly utilized without substantial loss in hydrogen production activity.

2. Experiments

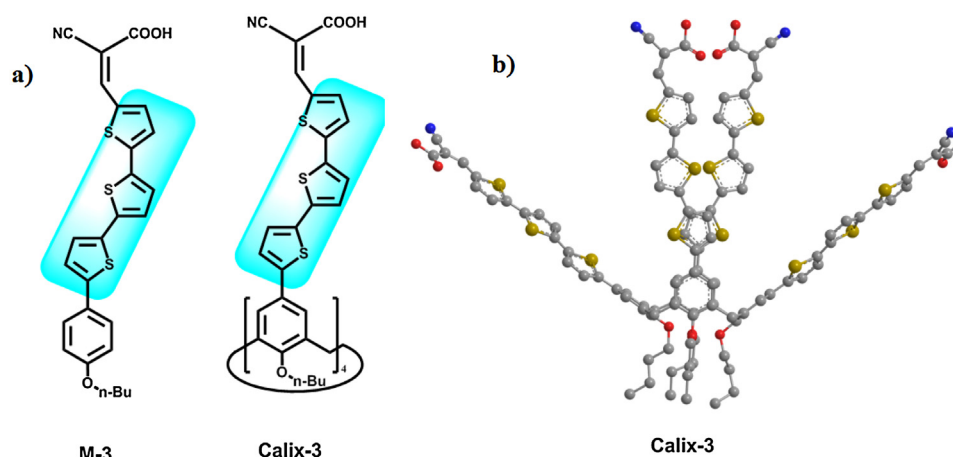
2.1. Preparation of photocatalysts

2.1.1. Synthesis of UiO-66-NH_2 -1

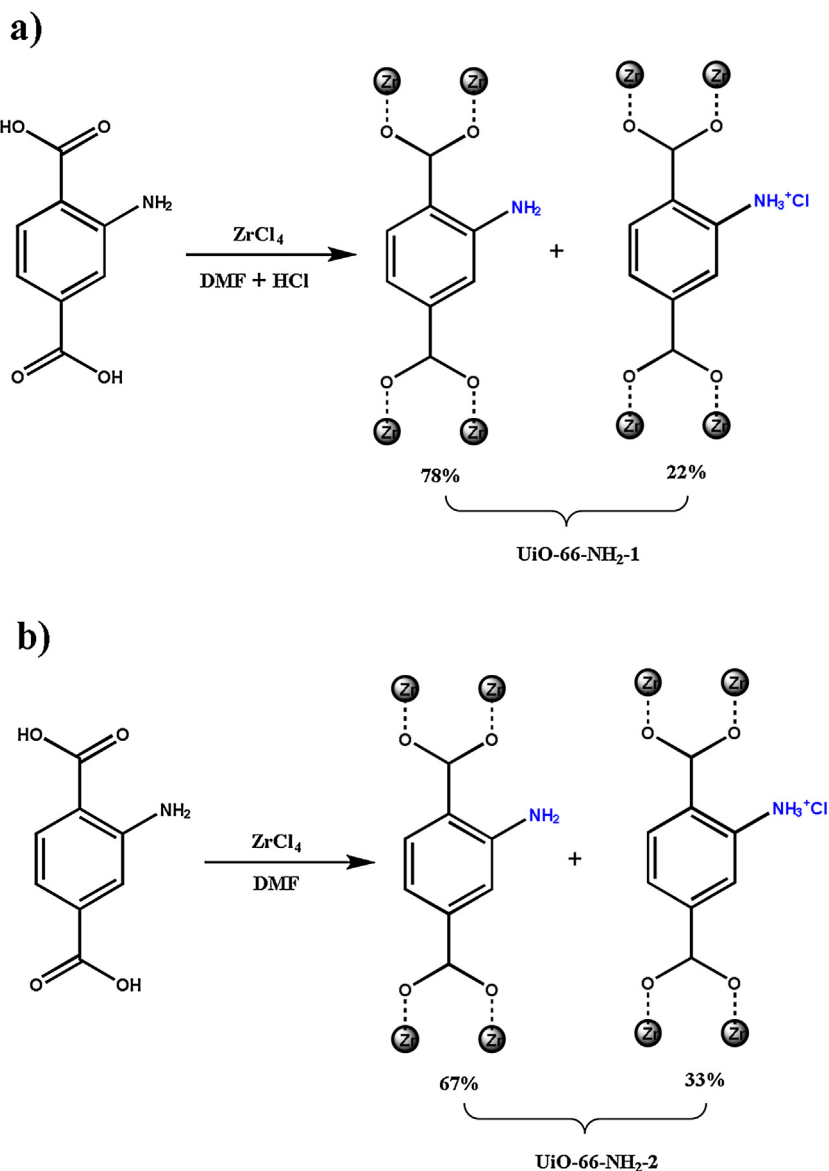
All reagents were analytical grade and were used without further purification. UiO-66-NH_2 -1 (Scheme 2a) was prepared following a modified procedure as described in literature [37]. In a typical synthetic process, a stainless steel vessel with Teflon liner containing ZrCl_4 (0.134 g, 0.575 mmol, pre-dissolved in 10 mL of DMF and 1 mL HCl) and 2-amino-1,4-benzenedicarboxylic acid ($\text{H}_2\text{BDC-NH}_2$, 0.125 g, 0.70 mmol, pre-dissolved in 5 mL of DMF) was heated at 80°C overnight. The resulting yellow crystalline powder was filtered out, washed with DMF ($3 \times 30 \text{ mL}$) and MeOH ($3 \times 30 \text{ mL}$), and then dried in air at 90°C .

2.1.2. Synthesis of UiO-66-NH_2 -2

UiO-66-NH_2 -2 (Scheme 2b) was prepared following a modified procedure as described in literature [38]. UiO-66-NH_2 -2 was synthesized by adding solution mixtures of ZrCl_4 (0.106 g, 0.454 mmol) in 50 mL of *N,N*-dimethylformamide (DMF) and 2-amino-1,4-benzenedicarboxylic acid ($\text{H}_2\text{BDC-NH}_2$, 0.081 g, 0.454 mmol) in 30 mL of DMF. Each of the mixtures was sonicated to dissolve the respective components. The solutions were then sealed in a stainless steel vessel with Teflon liner and heated to 120°C for 24 h. The resulting yellow crystalline powder was filtered out, washed with DMF ($3 \times 30 \text{ mL}$) and MeOH ($3 \times 30 \text{ mL}$), and then dried in air at 90°C .



Scheme 1. a) structures of **Calix-3** and comparison dye **M-3** and b) the optimized structure of cone-calixarene-based dye **Calix-3**.



Scheme 2. Synthesis of a) UiO-66-NH₂-1 and b) UiO-66-NH₂-2.

2.1.3. Synthesis of Pt@UiO-66-NH₂

Pt nanoparticles were introduced to UiO-66-NH₂ in amounts of 0.28 wt%, 0.65 wt% and 0.87 wt% (determined by the inductively coupled plasma atomic emission spectrometry, ICP-AES), respectively. In general, 1 g of UiO-66-NH₂ was dispersed in 100 mL aqueous solution containing a certain amount of K₂PtCl₆ and stirred for 6 h. After that, ascorbic acid was added following by 12 h for stirring. The solid was filtered out, washed and dried in vacuum oven at room temperature.

2.1.4. Synthesis of dye-sensitized Pt@UiO-66-NH₂

The catalysts were dispersed in 150, 200, and 250 ppm solution of CHCl₃ and DMF (v/v = 9:1) of **Calix-3**, or 200 and 800 ppm solution of CHCl₃ and DMF (v/v = 9:1) of **M-3** for 24 h, respectively. The red solids were filtered out, washed with CH₂Cl₂ until no colors was observed from the eluent and dried in vacuum oven at room temperature. The concentrations of dye solutions before and after use were determined by UV-vis spectra at 554 nm wavelength to calculate the adsorbing capacities of the catalysts.

2.2. Characterizations

The absorption spectra were observed with a Shimadzu UV-3600 spectrometer and fluorescence spectra were measured with an Edinburgh Instruments Ltd FLS980 spectrometer. Powder X-ray diffraction (XRD) was recorded on a Rigaku Smart Lab diffractometer (Bragg-Brentano geometry, Cu-K α radiation, $\lambda = 1.54056 \text{ \AA}$). Transmission electron microscopy (TEM) images, high-resolution transmission electron microscopy (HRTEM), high-angle annular dark field scanning transmission electron microscopy (HAADF-STEM) micrographs, and EDX elemental mapping were obtained by a JEM-2100F transmission electron microscope at 200 kV. Scanning electron microscope (SEM) micrographs were recorded on Hitachi Ultra-high Resolution FE-SEM SU8010 microscope. Cross-polarization magic-angle-spinning (CP/MAS) ¹³C/¹⁵N NMR spectroscopy was performed on a Bruker Ascend 300 MHz spectrometer (MAS probe with 4 mm outside diameter, zirconia rotors, and the ¹⁵N chemical shifts were given relative to liquid N₂ at zero ppm). Gas adsorption measurements were performed using

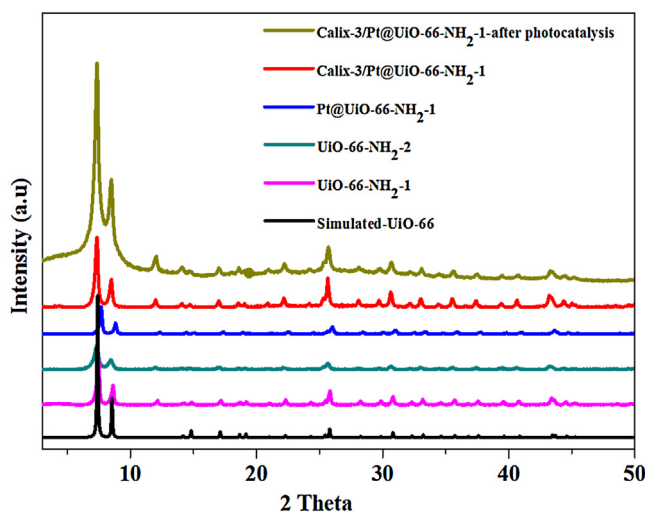


Fig. 1. PXRD patterns of two powdered UiO-66-NH₂, Pt@UiO-66-NH₂-1, and Calix-3/Pt@UiO-66-NH₂-1 with 0.65 wt% Pt loading before and after photocatalysis.

ultra-high purity N₂ gas on Quantachrome Auto-sorb-iQ2-MP analyzer. The Mott-Schottky curves were measured using a CHI760E electrochemical analyzer (China) in a three-electrode cell. Pt plate was used as counter electrode and Ag/AgCl electrode (3 M KCl) was used as reference electrode. The electrolyte was a 0.2 M Na₂SO₄ solution. The working electrode was prepared on fluorine-doped tin oxide (FTO) glass by dipping the mixed slurry containing the sample and H₂O on it, and the exposed area of the electrode was 0.25 cm². The photocatalytic hydrogen production system was Perfect Light Lab Solar-IIIAG and H₂ measurement was performed on Agilent Technologies 78. Apparent quantum yields (AQYs) were determined using a 420 nm or 450 nm band pass filter and an irradiation meter, and were calculated by the following equation: AQY(%)=(2 × The number of evolved H₂ molecules/The number of incident photons) × 100.

2.3. Photocatalytic hydrogen production

The photocatalytic hydrogen evolution by water splitting was performed in a glass reaction cell with quartz cover connected to a closed gas circulation which was swept by high purity N₂ before illumination. 25 mg photocatalyst was dispersed in 100 mL of 20 vol% MeOH aqueous solution (pH = 7.0). Then the suspension was exposed to a 300 W Xe lamp equipped with an optical filter ($\lambda > 420$ nm) to cut off the light in the ultraviolet region. The reaction solution was stirred continuously and cooled to room temperature by a circulation of cooling water. The amount of hydrogen evolved was determined at an interval of 1 h with online gas chromatography.

3. Results and discussion

3.1. Sample characterizations

UiO-66-NH₂-1 and UiO-66-NH₂-2 were prepared by a solvent-thermal route with and without HCl, respectively, in order to tune protonation of the –NH₂ groups on the porous framework (**Scheme 2**). The XRD patterns and SEM images of two UiO-66-NH₂ MOFs were recorded (**Fig. 1** and **Fig. S1**), which were consistent with the results of previous reports [37,38], denoting formation of isoreticular MOFs. Nitrogen adsorption-desorption isotherms measured at 77 K gave Brunauer-Emmett-Teller (BET) surface areas of 980 and 880 m² g⁻¹ for UiO-66-NH₂-1 and UiO-66-NH₂-2, respectively (**Fig. S2** and **Table S1**), confirming their similar porous structures. To unveil the protonation difference of the –NH₂ groups in these two isoreticular MOFs, further characterization was performed by CP/MAS ¹³C and ¹⁵N NMR spectra. The solid-state ¹³C NMR spectra showed resembling resonances at 170 ppm for the carbonyl carbon atoms and 148, 136, 130 and 115 ppm for the aromatic carbon atoms of the phenylene links (**Fig. S3**) in two MOFs. However, the solid-state ¹⁵N NMR spectra, which were obtained from analogous UiO-66-¹⁵NH₂ MOFs synthesized from ¹⁵N-enriched H₂BDC-¹⁵NH₂ (**Fig. S4a-b**), displayed two different resonances at about 68 and 139 ppm, which can be attributed to the free aromatic amine and the protonated amine salt –NH₃⁺Cl⁻, respectively [39]. Integration of direct-excitation NMR gave approximate ratios of 3.6:1 and 2.0:1 of free amine and protonated amine for UiO-66-NH₂-1 and UiO-66-NH₂-2 (**Scheme 2**), respectively. Considering larger surface areas and higher free amine amounts, we selected UiO-66-NH₂-1 as the main studied MOF.

Pt was introduced into by reduction of H₂PtCl₆ with ascorbic acid. The typical TEM images of the Pt@UiO-66-NH₂-1 with 0.65 wt% Pt loading showed the size distribution of Pt particles over UiO-66-NH₂-1 was about 3–5 nm (**Fig. 2a**). Analysis of HRTEM images of the Pt NPs indicated that the *d*-spacing between two adjacent lattice planes was about 0.196 nm, in agreement with the spacing of Pt(200) plane (**Fig. 2b**). Moreover, the composition of the Pt@MOF structure was particularly obvious in the HAADF-STEM images, in which Pt NPs appeared with brighter contrast due to larger atomic mass (**Fig. 2c**). The corresponding elemental mapping indicated the elements C, N, O, and Zr of UiO-66-NH₂ were homogeneously distributed throughout the whole MOFs (**Fig. S5**). The corresponding EDX results of a point analysis further demonstrated the existence of Pt NPs encapsulated in MOFs (**Fig. S6**). In addition, solid-state ¹⁵N NMR spectra of UiO-66-NH₂-1 and UiO-66-NH₂-2 showed the ratios of the free amine and protonated amine were 3.4:1 and 2.5:1, respectively, after the reaction with ascorbic acid (**Fig. S4c-d**).

The UV-vis spectrum showed that both UiO-66-NH₂ had a strong absorption peak at 375 nm with an absorption edge of 450 nm, corresponding to a 2.68 and 2.61 eV band gap for UiO-66-NH₂-1

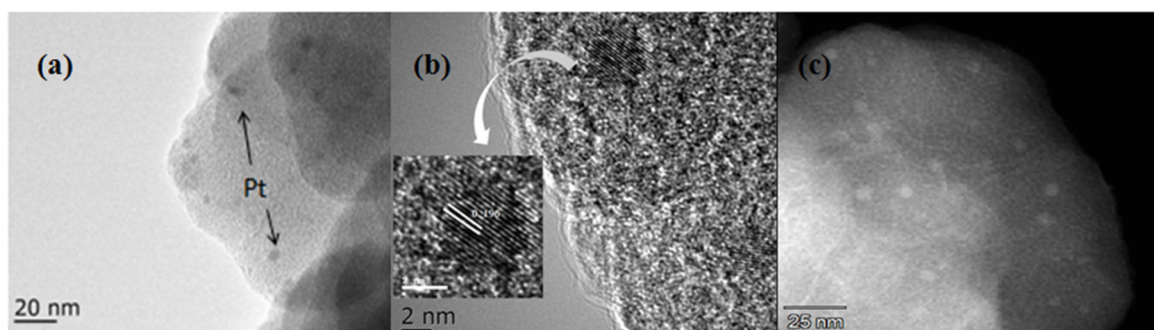


Fig. 2. (a) TEM, (b) HR-TEM and (c) HAADF-STEM image of Pt@UiO-66-NH₂-1 showing Pt NPs.

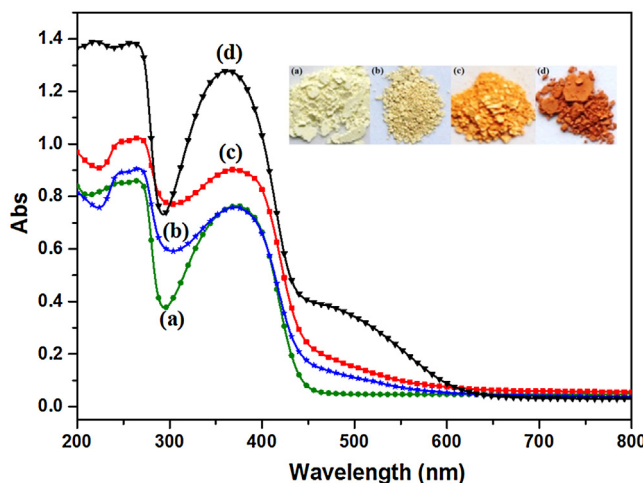


Fig. 3. UV-vis diffraction spectra of (a) UiO-66-NH_2 -1, (b) Pt@UiO-66-NH_2 -1, (c) $\text{M-3/Pt@UiO-66-NH}_2$ -1 and (d) $\text{Calix-3/Pt@UiO-66-NH}_2$ -1 with 0.65 wt% Pt loading (inset shows photographs of a, b, c and d).

and -2, respectively (Fig. 2 and Fig. S7). This allowed for promoting the charge separation with electrons populating the lowest unoccupied molecular orbital (LUMO) and holes in the highest occupied molecular orbital (HOMO) upon efficient light irradiation, owing to the semiconductor character of UiO-66-NH_2 . To elucidate the possibility for subsequent photocatalytic hydrogen production, Mott-Schottky measurements on UiO-66-NH_2 were conducted at frequencies of 1000 and 1500 Hz, respectively. As shown in Fig. 3, the positive slope of the obtained C^{-2} to the potential plot was in accordance with that of typical n-type semiconductors. The flat band position determined from the intersection was approximately -0.80 and -0.85 V vs. Ag/AgCl (i.e. -0.60 and -0.65 V vs. NHE) for UiO-66-NH_2 -1 and -2, respectively. Since it is generally accepted that the bottom of LUMO in n-type semiconductors was approximately equal to the flat-band potential [8], the LUMO of UiO-66-NH_2 -1 and -2 was estimated to be -0.60 and -0.65 V vs. NHE, which was more negative than the redox potential of H^+/H_2 . And then the HOMOs can be calculated to be 2.08 and 1.96 V vs. NHE for UiO-66-NH_2 -1 and -2 based on the band gap as described above, respectively. In our reported literature [36], the redox potentials of excited **Calix-3*** and **M-3*** (-1.00 and -1.40 V vs. NHE, respectively) were higher than the potential of LUMO in UiO-66-NH_2 . Therefore, it was thermodynamically favorable for direct electron transfer from **Calix-3*** or **M-3*** to UiO-66-NH_2 , which led to the proton reduction to realize photocatalytic H_2 generation.

The incorporation of Pt NPs contributed to the increase of light absorption intensity of UiO-66-NH_2 in the visible-light region, which was consistent with the color alteration of the powder from light yellow to dark yellow (Fig. 3). This observation clearly indicated the successful preparation of Pt@UiO-66-NH_2 . After treatment of Pt@UiO-66-NH_2 with a CHCl_3 and DMF ($v/v = 9:1$) solution of **Calix-3**, the powder color changed to reddish brown and the color of a **Calix-3** solution gradually disappeared. A typical absorption band of $\text{Calix-3/Pt@UiO-66-NH}_2$ was significantly broadened in the region from 450 to 600 nm. In comparison with a solution of **Calix-3** (Fig. S8), the UV-vis spectrum of **Calix-3** adsorbed onto UiO-66-NH_2 showed a red-shift of the peak maxima, which resulted most likely from the interaction of the $-\text{COOH}$ moieties of **Calix-3** dye and $-\text{NH}_2$ groups of the MOFs. A similar change was observed upon addition of Pt@UiO-66-NH_2 to the CHCl_3 solution of **M-3**.

To elucidate the interaction between amino group in Pt@UiO-66-NH_2 and carboxylic acid group in calix[4]arene based dye, FT-IR spectra of **Calix-3** and $\text{Calix-3/Pt@UiO-66-NH}_2$ -1-200 have been measured (Fig. S9a). For the **Calix-3** powders, the alkyl $\text{C}-\text{H}$,

$\text{C}\equiv\text{N}$, and $\text{C}=\text{O}$ stretching bands were observed at 2956, 2360, and 1711 cm^{-1} , respectively. When the dyes were adsorbed on Pt@UiO-66-NH_2 surface, the alkyl $\text{C}-\text{H}$ and $\text{C}\equiv\text{N}$ stretching bands still existed but $\text{C}=\text{O}$ stretching bands disappeared and instead peaks were found at 1690, 1650, and 1625 cm^{-1} , respectively. This indicates the formation of hydrogen bond between the $-\text{COOH}$ moieties of **Calix-3** dye and $-\text{NH}_2$ or $-\text{NH}_3^+$ groups of the MOFs, and the possible bond modes are presented in Fig. S9b. In addition, comparative studies in CP/MAS ^{15}N NMR of Pt@UiO-66-NH_2 before and after combination of calix[4]arene based dye have been studied (Fig. S4e-f). The surprising results showed the ratios of the free amine and protonated amine were improved to 7.6:1 and 5.0:1 for $\text{Calix-3/Pt@UiO-66-NH}_2$ -1 and $\text{Calix-3/Pt@UiO-66-NH}_2$ -2, respectively, probably for the strong interaction between **Calix-3** dye and Pt@UiO-66-NH_2 .

The relationships between the pore size of UiO-66-NH_2 and other segments, such as Pt particle size and molecular size of calix[4]arene based dye, have been also investigated. The synthesized UiO-66-NH_2 was composed of cubes in the scale of 60–80 nm (Fig. S1) and the structure of UiO-66-NH_2 was isostructural of UiO-66 , which was confirmed by PXRD results (Fig. 1). Fig. S10 shows pore size and octahedral Zr cluster of UiO-66 [38]. The images indicated pore side length and diagonal length were 11.13 and 15.74 Å, respectively, and the side length and diagonal length of octahedral Zr cluster were 3.51 and 4.96 Å, respectively. Considering the sizes of Pt particles over UiO-66-NH_2 were about 3–5 nm (Fig. 2), we deduced some particles were distributed throughout the volume of the MOF crystal but still exhibiting an average particle size exceeding the dimensions of the pores, and the other particles were larger than cavity size with a preferred anchoring close to the outer surface of the MOF (Fig. S11). In addition, the optimized geometries of **Calix-3** dyes were mimicked through molecular modelling with the GAUSSIAN 03 package. The cone conformation was clearly shown in Fig. S12 and the length of the thiophenyl chain was 14.53 Å. In addition, the optimized distance of the 1, 3-position or 2, 4-position carboxyl group at the upper rim of **Calix-3** was 33.77 Å and 6.73 Å, respectively, which could be adjusted to match the surroundings of Pt@MOF owing to the chain flexibility.

3.2. Effect of Pt loading on photocatalytic H_2 production

In a dye-sensitized photocatalytic system, Pt NPs as a co-catalyst promoted the charge separation and decreased the low over potential for H_2 evolution. Meanwhile, dyes absorbed visible light and formed electronically excited states to transfer electron. Both Pt NPs and dyes have a synergistic effect on the photocatalytic activities of the catalysts. Pt@UiO-66-NH_2 -1 were sensitized by using 150, 200 and 250 ppm CHCl_3 solution of **Calix-3** (denoted $\text{Calix-3/Pt@UiO-66 NH}_2$ -1-X, X = 150, 200, 250), and the adsorbed amounts of dyes in these catalysts were listed in Table S2, respectively. The full-light driven photocatalytic processes of Pt@UiO-66-NH_2 -1 with methanol as an electron donor were employed to investigated the influence of different Pt loadings (0.28 wt%, 0.65 wt% and 0.87 wt%) on H_2 generation. As illustrated in Fig. S13, when 0.65 wt% of Pt NPs were incorporated, Pt@UiO-66-NH_2 -1 showed a maximum rate of $220\text{ }\mu\text{mol g}^{-1}\text{ h}^{-1}$ for H_2 production. Further study on the visible-light driven ($\lambda \geq 420\text{ nm}$) photocatalytic H_2 generation of $\text{Calix-3/Pt@UiO-66-NH}_2$ -1-200 with different Pt loadings were also carried out. Fig. S14 shows an optimum H_2 evolution rate of $1528\text{ }\mu\text{mol g}^{-1}\text{ h}^{-1}$ based on the whole catalyst mass (i.e. $236\text{ mmol g}^{-1}[\text{Pt}]$ h^{-1} based on Pt mass or $49\text{ mmol g}^{-1}[\text{Calix}]$ h^{-1} based on **Calix-3** dye mass) was achieved when using 0.65 wt% of Pt loadings. To the best of our knowledge, the H_2 evolution value is actually quite high considering the extremely low Pt loadings, and is higher than those produced by most of the previously reported

MOF-based photocatalysts [40]. Thus, the optimized Pt loading was selected to be 0.65 wt% herein below.

3.3. Effect of dye-adsorbed amount on photocatalytic H_2 production

The photocatalytic activities of the Calix-3/Pt@UiO-66-NH₂-1 catalysts were evaluated in the visible light region. As shown in Fig. S15, Calix-3/Pt@UiO-66-NH₂-1-150 exhibited a photocatalytic activity of 894 $\mu\text{mol g}^{-1} \text{h}^{-1}$. With the concentration increase of **Calix-3** to 200 ppm, the best photocatalytic activity of 1528 $\mu\text{mol g}^{-1} \text{h}^{-1}$ was obtained. However, further increase in concentration to 250 ppm resulted in the activity decrease of 964 $\mu\text{mol g}^{-1} \text{h}^{-1}$, suggesting the activities of the catalysts were not positively correlated to the dye-adsorbed amounts. It can be explained that when too much dye was adsorbed onto the catalyst, the excessive dye molecules might cause a loss of light harvesting and block effective electron transport simultaneously. In contrast, when no dyes were adsorbed onto Pt@UiO-66-NH₂-1 with 0.65 wt% Pt loading, the H_2 generation rate was low as expected (55 $\mu\text{mol g}^{-1} \text{h}^{-1}$ or 8.5 $\text{mmol g}^{-1} [\text{Pt}] \text{h}^{-1}$), which was comparable to that (257.38 $\mu\text{mol g}^{-1} \text{h}^{-1}$ or 9.0 $\text{mmol g}^{-1} [\text{Pt}] \text{h}^{-1}$) of Pt@UiO-66-NH₂ with 2.87 wt% Pt loading reported by Jiang et al. [8], indicating most of Pt nanoparticles were incorporated inside UiO-66-NH₂-1 for photocatalytic hydrogen production. The above results showed that **Calix-3** could sensitize UiO-66-NH₂-1 effectively and its adsorbed amounts had an important influence on the photocatalytic activity.

3.4. Effect of dye-MOF interaction on photocatalytic H_2 production

To investigate the effect of two different UiO-66-NH₂ MOFs prepared with and without HCl on the photocatalytic activities, control experiments using Calix-3/Pt@UiO-66-NH₂-2-200 were carried out. It was found that the catalyst based on UiO-66-NH₂-2 gave lower amounts of H_2 (1000 $\mu\text{mol g}^{-1} \text{h}^{-1}$) after visible-light irradiation under the same photocatalytic conditions, compared with that based on UiO-66-NH₂-1 (Fig. 5). Considering the two catalysts had close dye-adsorbed amounts and conduction band (LUMO) (Fig. 4 and Table S2), the decrease in H_2 production could be caused by the weaker interaction of the **Calix-3** and UiO-66-NH₂-2 because the more $-\text{NH}_3^+$ groups in UiO-66-NH₂-2 were disadvantageous to the forming of strong dual hydrogen bond between the $-\text{COOH}$ moieties of **Calix-3** dye and $-\text{NH}_2$ groups of the MOFs. We proposed that when dyes were more stably fixed on MOFs by stronger bond, they could serve as light-absorbing molecules to ensure more effective electron transfer between the dye and surrounding MOF, and thereby leading to the increase of H_2 production.

3.5. Effect of the dyes **calix-3** and **M-3** on photocatalytic H_2 production

The H_2 production rates with two **M-3**-sensitized catalysts M-3/Pt@UiO-66-NH₂-1-200 and M-3/Pt@UiO-66-NH₂-1-800 with 0.65 wt% Pt loading were also examined under the same conditions. As shown in Fig. 5, M-3/Pt@UiO-66-NH₂-1-200 exhibited a photocatalytic activity of 267 $\mu\text{mol g}^{-1} \text{h}^{-1}$, which was only one third of that catalyzed by Calix-3/Pt@UiO-66-NH₂-1-200. It was worth noting that M-3/Pt@UiO-66-NH₂-1-800 also showed a lower activity of 516 $\mu\text{mol g}^{-1} \text{h}^{-1}$ despite the fact that the catalysts contained the similar amounts of light-harvesting units adsorbed onto Pt@UiO-66-NH₂-1 as those of Calix-3/Pt@UiO-66-NH₂-1-200 (Table S2). The results may be rationalized by the following reasons: **Calix-3** had four D- π -A units per molecule, which were not only favorable to

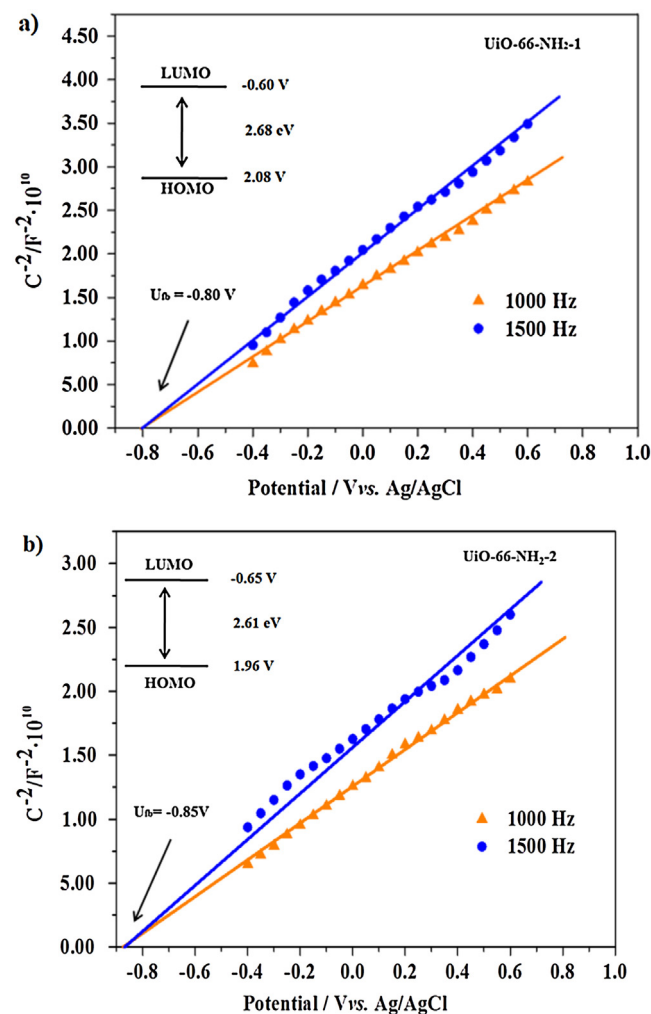


Fig. 4. Mott-Schottky plot of (a) UiO-66-NH₂-1 and (b) UiO-66-NH₂-2 in 0.2 M Na_2SO_4 aqueous solution.

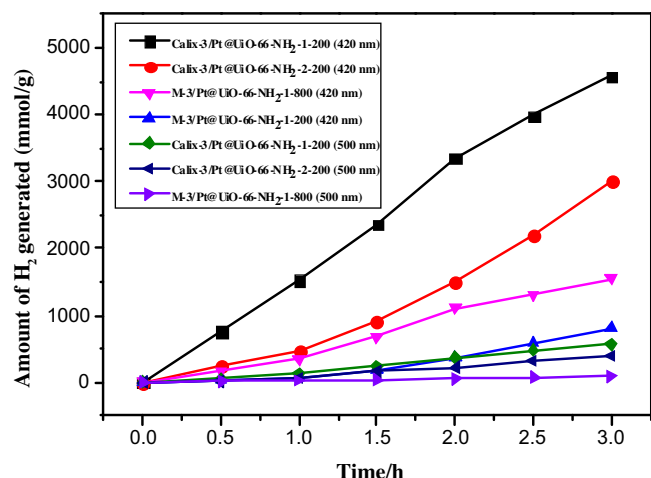


Fig. 5. Photocatalytic H_2 production over Calix-3/Pt@UiO-66-NH₂-1, Calix-3/Pt@UiO-66-NH₂-2, and M-3/Pt@UiO-66-NH₂-1 with 0.65 wt% Pt loading under visible light irradiation ($\lambda > 420 \text{ nm}$ or $\lambda > 500 \text{ nm}$).

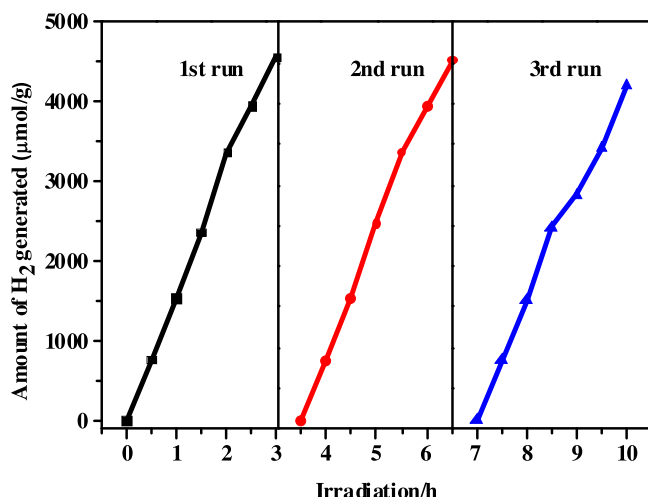


Fig. 6. Photocatalytic H₂ production over the recyclability of Calix-3/Pt@UiO-66-NH₂-1 with 0.65 wt% Pt loading under visible light irradiation.

achieve high molar extinction coefficients but also promoted effective electron transfer between the dye and MOF.

3.6. Effect of irradiation wavelength on photocatalytic H₂ production

Photocatalytic H₂ production with the catalysts Calix-3/Pt@UiO-66-NH₂-1-200, Calix-3/Pt@UiO-66-NH₂-2-200 and M-3/Pt@UiO-66-NH₂-2-800 were performed under visible light irradiation using colored filters with different cutoff wavelengths ($\lambda > 420$ nm and > 500 nm) [41]. Compared with H₂ production rate under visible light irradiation ($\lambda > 420$ nm), the production rates for Calix-3/Pt@UiO-66-NH₂-1-200, Calix-3/Pt@UiO-66-NH₂-2-200 and M-3/Pt@UiO-66-NH₂-2-800 rapidly fell to 12%, 13%, and 10%, respectively, under irradiation at wavelengths longer than 500 nm (Fig. 5). These results suggest that H₂ formation depends on the absorption range of dyes. In our system, **Calix-3** and **M-3** exhibit their visible absorption peaks at about 450 nm and thus have weak absorption at wavelengths longer than 500 nm, leading to the decrease of H₂ production rate. The apparent quantum yields were determined to be 2.3% at 420 nm and 1.8% at 450 nm for Calix-3/Pt@UiO-66-NH₂-1-200 (Table S3).

3.7. Stability tests

The loss in H₂ production rate is a common problem in dye-sensitization system, which could be caused by the dye consumption or instability under long time visible light irradiation. The photocatalytic performance of Calix-3/Pt@UiO-66-NH₂-1-200 was repeatedly evaluated to confirm the stability in this reaction. As shown in Fig. 1, no obvious change in XRD patterns of the catalysts was observed after three consecutive usages for H₂ generation, indicating excellent stability of UiO-66-NH₂-1. More importantly, the catalyst was recyclable at least three times without a distinct decrease in photocatalytic performance for formation of H₂ under visible light irradiation, further verifying the good intrinsic and adsorbed stability of **Calix-3** (Fig. 6). The high turnover number (TON) based on Pt or **Calix-3** content achieved for H₂ evolution was 400 (Pt-TON) or 846 (Calix-3-TON) after 9 h, respectively.

3.8. Mechanism of enhanced photocatalytic H₂ production

To study the photocatalysis mechanism, the steady-state photoluminescence (PL) spectra were measured to monitor the electron

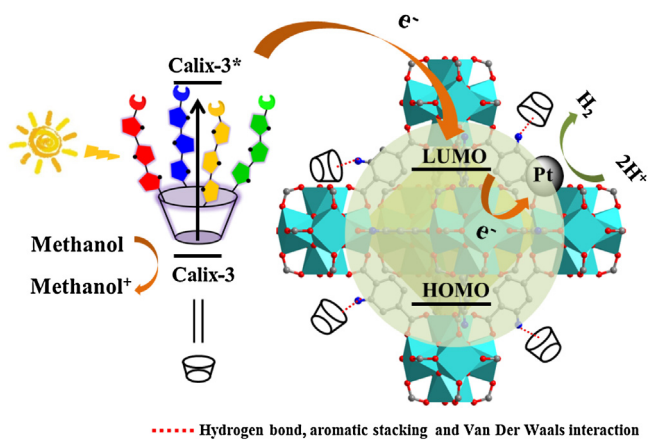


Fig. 7. Proposed mechanism of photocatalytic H₂ production over **Calix-3** sensitized Pt@UiO-66-NH₂ under visible light irradiation.

transfer from the excited **Calix-3** to UiO-66-NH₂ (Fig. S16). The **Calix-3** solid showed an intensive emission peak centered at 745 nm, which was ascribed to its strong recombination of excited charge pairs by exciting light. When Calix-3/Pt@UiO-66-NH₂-1-200 was measured under the same conditions, a significant decrease in the peak intensity of **Calix-3** emission and concomitantly slight blue shifts (~ 37 nm) of the emission peak were observed, which could be mainly ascribed to the interfacial electron transfer from the attached **Calix-3*** to the UiO-66-NH₂ frameworks and the interaction of UiO-66-NH₂ with **Calix-3**. Then it was reasonable to assume that the electron transferred from excited **Calix-3** to UiO-66-NH₂ through the hydrogen bonds and π - π interactions, and finally electron transferred to Pt surface to produce H₂ (Fig. 7). On the other hand, to determine the hydrogen precursor, a controlled experiment with D₂O solution containing 20 vol% MeOH as sacrificial electron donors confirmed that all evolved hydrogen was D₂, ensuring the hydrogen source was the protons in the water not from other compounds, such as donor species or dye-sensitizers.

4. Conclusions

A novel cone-calix[4]arene compound **Calix-3** containing four D- π -A units was successfully used as a sensitizer to extend the photoresponse of Zr-containing based MOF (UiO-66-NH₂) embedded with Pt particles into visible light region. A significant improved hydrogen production activity ($1528 \mu\text{mol g}^{-1} \text{h}^{-1}$, $236 \text{ mmol g}^{-1} [\text{Pt}] \text{h}^{-1}$, or $49 \text{ mmol g}^{-1} [\text{Calix}] \text{h}^{-1}$) and stability (Pt-TON = 400, or Calix-3-TON = 846 for 9 h) for **Calix-3**-sensitized Pt@UiO-66-NH₂ catalysts were realized compared to the corresponding systems sensitized by single D- π -A **M-3** and most of the previously reported MOF-based photocatalysts, which may be due to lower tendency for aggregation, higher molar absorption coefficients, more efficient electron transfer, and better intrinsic and adsorbed stability of **Calix-3** dyes. Given the low cost and easy operation of present H₂ production system, this study provides a potential approach to develop highly efficient MOF-based photocatalysts for hydrogen production.

Acknowledgements

This work was supported by the NSFC Projects (91222201, 21572280, 61370059, 21573291), STP Project of Guangzhou (15020016), NSF of Beijing (4152030) and NSF of Guangdong Province (S2013030013474).

Appendix A. Supplementary data

Supplementary data associated with this article can be found, in the online version, at <http://dx.doi.org/10.1016/j.apcatb.2017.01.040>.

References

- [1] Z. Zou, J. Ye, K. Sayama, H. Arakawa, *Nature* 414 (2001) 625–627.
- [2] A.J. Eisswein, D.G. Nocera, *Chem. Rev.* 107 (2007) 4022–4047.
- [3] A. Kudo, Y. Miseki, *Chem. Soc. Rev.* 38 (2009) 253–278.
- [4] T. Zhang, W. Lin, *Chem. Soc. Rev.* 43 (2014) 5982–5993.
- [5] D.Z. Zee, T. Chantarojsiri, J.R. Long, C.J. Chang, *Acc. Chem. Res.* 48 (2015) 2027–2036.
- [6] V.S. Vyas, F. Haase, L. Stegbauer, G. Savasci, F. Podjaski, C. Ochsenfeld, B.V. Lotsch, *Nat. Commun.* 6 (2015) 8508–8516.
- [7] Q. Lin, X. Bu, C. Mao, X. Zhao, K. Sasan, P. Feng, *J. Am. Chem. Soc.* 137 (2015) 6184–6187.
- [8] J.-D. Xiao, Q. Shang, Y. Xiong, Q. Zhang, Y. Luo, S.-H. Yu, H.-L. Jiang, *Angew. Chem. Int. Ed.* 55 (2016) 9389–9393, *Angew. Chem.* 128 (2016) 9535–9539.
- [9] B. Chen, S. Xiang, G. Qian, *Acc. Chem. Res.* 43 (2010) 1115–1124.
- [10] H.-C. Zhou, J.R. Long, O.M. Yaghi, *Chem. Rev.* 112 (2012) 673–674.
- [11] H.-C. Zhou, S. Kitagawa, *Chem. Soc. Rev.* 43 (2014) 5415–5418.
- [12] S. Wang, W. Yao, J. Lin, Z. Ding, X. Wang, *Angew. Chem. Int. Ed.* 53 (2014) 1034–1038, *Angew. Chem.* 126 (2014) 1052–1056.
- [13] L. Shi, T. Wang, H. Zhang, K. Chang, J. Ye, *Adv. Funct. Mater.* 25 (2015) 5360–5367.
- [14] H.-Q. Xu, J. Hu, D. Wang, Z. Li, Q. Zhang, Y. Luo, S.-H. Yu, H.-L. Jiang, *J. Am. Chem. Soc.* 137 (2015) 13440–13443.
- [15] Y.-P. Yuan, L.-S. Yin, S.-W. Cao, G.-S. Xu, C.-H. Li, C. Xue, *Appl. Cata. B: Environ.* 168–169 (2015) 572–576.
- [16] C. Gomes Silva, I. Luz, F.X.L. Xamena, A. Corma, H. García, *Chem.- Eur. J.* 16 (2010) 1133–11138.
- [17] S. Pullen, H. Fei, A. Orthaber, S.M. Cohen, S. Ott, *J. Am. Chem. Soc.* 135 (2013) 16997–17003.
- [18] S. Saha, G. Das, J. Thote, R. Banerjee, *J. Am. Chem. Soc.* 136 (2014) 14845–14851.
- [19] T. Zhou, Y. Du, A. Borgna, J. Hong, Y. Wang, J. Han, W. Zhang, R. Xu, *Energy Environ. Sci.* 6 (2013) 3229–3234.
- [20] X.-Y. Dong, M. Zhang, R.-B. Pei, Q. Wang, D.-H. Wei, S.-Q. Zang, Y.-T. Fan, T.C.W. Mak, *Angew. Chem. Int. Ed.* 55 (2016) 2073–2077, *Angew. Chem.* 128 (2016) 2113–2117.
- [21] X.-J. Kong, Z. Lin, Z.-M. Zhang, T. Zhang, W. Lin, *Angew. Chem. Int. Ed.* 55 (2016) 6521–6526, *Angew. Chem.* 128 (2016) 6521–6526.
- [22] H.-Q. Xu, J. Hu, D. Wang, Z. Li, Q. Zhang, Y. Luo, S.-H. Yu, H.-L. Jiang, *J. Am. Chem. Soc.* 137 (2015) 13440–13443.
- [23] T. Zhang, W. Lin, *Chem. Soc. Rev.* 43 (2014) 5982–5993.
- [24] W. Zhen, J. Ma, G. Lu, *Appl. Cata. B: Environ.* 190 (2016) 12–25.
- [25] J. Zhao, Y. Wang, J. Zhou, P. Qi, S. Li, K. Zhang, X. Feng, B. Wang, C. Hu, *J. Mater. Chem. A* 4 (2016) 7174–7177.
- [26] C. Wang, K.E. deKrafft, W. Lin, *J. Am. Chem. Soc.* 134 (2012) 7211–7214.
- [27] M. Wen, K. Mori, T. Kamegawa, H. Yamashita, *Chem. Commun.* 50 (2014) 11645–11648.
- [28] M.A. Nasalevich, R. Becker, E.V. Ramos-Fernandez, S. Castellanos, S.L. Veber, M.V. Fedin, F. Kapteijn, J.N.H. Reek, J.I. van der Vlugt, J. Gascon, *Energy Environ. Sci.* 8 (2015) 364–375.
- [29] J. He, J. Wang, Y. Chen, J. Zhang, D. Duan, Y. Wang, Z. Yan, *Chem. Commun.* 50 (2014) 7063–7066.
- [30] W.J. Youngblood, S.H.A. Lee, K. Maeda, T.E. Mallouk, *Acc. Chem. Res.* 42 (2009) 1966–1973.
- [31] S.X. Min, G.X. Lu, *J. Phys. Chem. C* 116 (2012) 19644–19652.
- [32] Y. Wang, J.D. Hong, W. Zhang, R. Xu, *Catal. Sci. Technol.* 3 (2013) 1703–1711.
- [33] S.X. Min, G.X. Lu, *J. Phys. Chem. C* 115 (2011) 13938–13945.
- [34] J. He, J.Q. Wang, Y.J. Chen, J.P. Zhang, D.L. Duan, Y. Wang, Z.Y. Yan, *Chem. Commun.* 50 (2014) 7063–7066.
- [35] H. Tributsch, *Coord. Chem. Rev.* 248 (2004) 1511–1530.
- [36] L.-L. Tan, J.-M. Liu, S.-Y. Li, L.-M. Xiao, D.-B. Kuang, C.-Y. Su, *ChemSusChem* 8 (2015) 280–287.
- [37] M.J. Katz, Z.J. Brown, Y.J. Colon, P.W. Siu, K.A. Scheidt, R.Q. Snurr, J.T. Hupp, O.K. Farha, *Chem. Comm.* 49 (2013) 9449–9451.
- [38] J.H. Cavka, S. Jakobsen, U. Olsbye, N. Guillou, C. Lamberti, S. Bordiga, K.P. Lillerud, *J. Am. Chem. Soc.* 130 (2008) 13850–13851.
- [39] W. Morris, C.J. Doonan, O.M. Yaghi, *Inorg. Chem.* 50 (2011) 6853–6855.
- [40] A. Dhakshinamoorthy, A.M. Asiri, Hermenegildo García, *Angew. Chem. Int. Ed.* 55 (2016) 5414–5445, *Angew. Chem.* 128 (2016) 5504–5535.
- [41] T. Kamegawa, S. Matsuura, H. Seto, H. Yamashita, *Angew. Chem. Int. Ed.* 52 (2013) 916–919, *Angew. Chem.* 125 (2013) 950–953.